



# Hybrid heterostructures based on hematite and highly hydrophilic carbon dots with photocatalytic activity

Tiago Cabral Araújo<sup>a</sup>, Henrique dos S. Oliveira<sup>b</sup>, José Joaquim Sá Teles<sup>a</sup>, Jose Domingos Fabris<sup>a</sup>, Luiz C.A. Oliveira<sup>b</sup>, João Paulo de Mesquita<sup>a,\*</sup>

<sup>a</sup> Department of Chemistry—Federal University of Jequitinhonha and Mucuri Valleys, Rodovia MGT 367—Km 583, n° 5000, Alto da Jacuba, CEP 39100-000 Diamantina, MG, Brazil

<sup>b</sup> Department of Chemistry—Federal University of Minas Gerais, Av. Antônio Carlos, 6627, CEP 31270-901, Pampulha, Belo Horizonte, MG, Brazil

## ARTICLE INFO

### Article history:

Received 2 May 2015

Received in revised form 26 August 2015

Accepted 15 September 2015

Available online 18 September 2015

### Keywords:

Carbon dots

Hematite

Hybrid heterostructures

Photocatalysis

## ABSTRACT

Highly hydrophilic carbon dots (HCD) prepared by dehydration and oxidation of cellulose were used in preparation of hybrid heterostructures with  $\alpha\text{Fe}_2\text{O}_3$  in aqueous medium. The nanostructures were characterized by different techniques including XRD, Mossbauer spectroscopy, TG, HRTEM, FTIR, Raman, potentiometry titration and cyclic voltammetry. The formation of a hybrid heterojunction was shown by determining the energy of the top of the valence band and the bottom of the conduction band through voltammetric measurements and electronic spectroscopy. These results indicate that the hybrid material exhibits Type II band offsets that are able to promote an efficient separation of photogenerated charges under irradiation of visible light. The photocatalytic activity of the heterojunction was evaluated in the photodegradation of indigo carmine dye. The high photocatalytic activity observed under visible light is discussed on basis of the coupling of the hybrid heterojunction band structure.

© 2015 Elsevier B.V. All rights reserved.

## 1. Introduction

Among the strategies to develop efficient visible light photocatalysts, the heterojunction or heterostructure concept has proven to be technologically feasible and chemically efficient alternative [1]. This concept has been reportedly improving the photocatalytic properties of different photocatalyst by increasing the efficiency of the light absorption, charge separation enhancement, increased reactions kinetics and interface electronic structure modification [2].

Iron oxides are a promising candidate for development of visible-light photocatalysis [3,4]. The oxides are *n*-type semiconductors with a small band gap ( $\sim 2.0\text{ eV}$ ), high stability under ambient conditions and aqueous solution at  $\text{pH} > 3$  and low toxicity; they absorb visible light and are a widely available source of semiconductor materials. Hematite ( $\alpha\text{Fe}_2\text{O}_3$ ) nanoparticles, for example, with large surface area and porous structure, have been prepared elsewhere and revealed to present distinguished photocatalytic activity [5,6]. Although having very promising results, this oxide has low charge carrier mobility ( $10^{-1}$  and  $10^{-2}\text{ cm}^2/\text{Vs}$ ) and

a fast recombination rate [7,8]. In addition, the diffusion length of the holes is extremely short, in the range of 2–4 nm, a value which is about one hundredth of that observed for other metal oxides [9]. Consequently, the obtained values of photocatalytic activity are lower than what would be usually expected for related semiconductors.

Obtaining heterojunctions has been an effective alternative to improve the chemical performance of photocatalysts based on iron oxides [10–13]. Recently, it was showed that the activity of the photocatalytic oxidation of water, as it was promoted by hematite ( $\alpha\text{Fe}_2\text{O}_3$ ) was greatly enhanced by incorporating iron oxide nanoparticles on reduced graphene oxide [14]. The authors showed that coupling the hematite nanoparticles with graphene oxide increases the photocurrent, reduces the charge recombination rate and that the photogenerated electrons are transferred from the  $\alpha\text{Fe}_2\text{O}_3$  to the graphene oxide.

Herein it is reported the preparation and characterization of a hybrid heterostructure of  $\alpha\text{Fe}_2\text{O}_3$  with highly hydrophilic carbon dots (HCD). Carbon dots (CDs) are the newest class of carbon-based nanoparticles discovered in 2004 during the electrophoretic purification of carbon nanotubes [15]. These materials are prepared usually with different precursors and techniques including pyrolysis and arc. [16]. They are materials considered as being promising candidates for the development of photocatalysts with adjustable

\* Corresponding author.

E-mail address: [joaopm2000@yahoo.com.br](mailto:joaopm2000@yahoo.com.br) (J.P. de Mesquita).

and strong chemical activity and high specificity and selectivity [17–24]. This potential is directly related to some of their characteristics; as they do not suffer photocorrosion, are inexpensive, easy to prepare, non toxic and environmentally friendly, if compared to other similar materials [18,25,26]. They are able to convert a longer-wavelength radiation (e.g., light NIR) into shorter wavelengths, such as visible light, and this makes them of great potential for being used in chemical catalysis and in energy conversion applications.

In this work, we have prepared a hybrid nanocomposite between  $\alpha\text{Fe}_2\text{O}_3$  and HCD. The HCD were obtained through the dehydration/oxidation reactions of cotton cellulose in an aqueous medium. The hybrid heterostructures between these two materials, hematite and HCD, were characterized through the analysis of the semiconductor band structures, with cyclic voltammetry and electronic spectroscopy. In addition, we show that the high catalytic activity is directly related to the band structure coupling of the material that increases the absorption efficiency of visible radiation and reduces the recombination rate of the electron-hole pair.

## 2. Experimental

### 2.1. Preparation of the carbon dots

The HCD was prepared as described in the literature with some modifications [27]. First, 5 g of cotton cellulose were dehydrated in 20 ml of  $\text{H}_2\text{SO}_4$  to 80 °C for 40 min. Following was interrupted by adding 100 ml of water. The obtained carbon material was washed with pure water and oxidized by  $\text{HNO}_3$  (2 M) in reflux for 12 h and the resulting solution neutralized with  $\text{Na}_2\text{CO}_3$  and dialyzed until constant conductivity, typically after 72 h.

### 2.2. Preparation of $\alpha\text{Fe}_2\text{O}_3$ and $\alpha\text{Fe}_2\text{O}_3/\text{HCD}$

The hematite ( $\alpha\text{Fe}_2\text{O}_3$ ) sample was prepared as described in Ref. [28]. In Brief, 30 ml of 1 M KOH and 5 ml of 1 M  $\text{NaHCO}_3$  were added to 50 ml of 0.28 M  $\text{Fe}(\text{NO}_3)_3 \cdot 9\text{H}_2\text{O}$  at 90 °C. The obtained mixture was refluxed under stirring for 3 days at a mean temperature of 90 °C. The solid so obtained was dried in oven for 24 h. To prepare the  $\alpha\text{Fe}_2\text{O}_3/\text{HCD}$  system, it was followed the same procedure as above except for dissolving the iron salt in the HCD solution.

### 2.3. Characterization of materials

The FTIR spectra were obtained in a Nicolet 380 FT-IR spectrometer (Nicolet, MN) using the attenuated total reflectance (ATR) accessory. The Micro-Raman spectra were obtained using a Senterra system with a 633 or 785 nm excitation wavelength. Measurements were made using a 50× objective lens, with laser powers ranging from 0.2 to 10 mW, and exposure times of 2–10 s. The diffuse reflectance spectra were obtained with a UV-vis spectrometer Shimadzu UV 2700. The Kubelka–Munk equation was used to manipulate all data. Photoluminescence (PL) emission measurements were performed using a Cary Eclipse Fluorescence spectrophotometer (Varian). XRD data were obtained in a Shimadzu model XRD6000 using  $\text{CuK}\alpha$  radiation scanning from 10 to 80° at a scan rate of 1° min<sup>−1</sup>. The measurements were performed with a current of 30 mA and a voltage of 30 kV. The mean crystallite size was calculated with the Scherrer equation. Potentiometric titration curves were performed at 25 °C using a Schott automatic titrator (Titroline 7000). 5.0 ml of HCD solution were added in 15.0 ml of a 0.0019 mol L<sup>−1</sup> HCl solution, directly into the electrochemical cell and titrated with a  $\text{CO}_2$ -free 0.0087 mol L<sup>−1</sup> NaOH solution with  $\text{N}_2$  purge. A nonlinear method for fitting acid-base potentiometric titration data was applied to determine the amount of acid groups on the surface of the materials [29,30]. The Zeta

potential ( $\xi$ -potential) values for the HCD were measured using a Zetasizer Nano-ZS (Malvern Instruments, U.K.). Transmission electron microscopy images of the HCD were taken using a FEI Tecnai G2-Spirit with 200 kV acceleration voltage. The HCD suspensions were deposited from an aqueous dispersion on carbon film coated electron microscopic grids. Scanning electron microscopy (SEM) images were taken by using a Quanta 200 FEG-FEI. Thermogravimetric analyses (TGA/DTG) were carried out using a Shimadzu equipment model DTG60 with approximately 10 mg of sample. The curves were obtained under a heating rate of 10 °C min<sup>−1</sup>. The  $\alpha$ -alumina was used as reference in the differential thermal analysis. The Cyclic voltammograms were obtained with a potentiostat Palm-Sens at room temperature using a conventional three electrode arrangement with a Pt wire counter electrode and an Ag/AgCl reference electrode (3.0 M KCl). The working electrode was prepared by deposition of materials ( $\alpha\text{Fe}_2\text{O}_3$ , HCD) on the surface of a glassy carbon electrode, previously polished with alumina powder, followed by sonication water and acetone. All electrochemical experiments in this work were performed in a 0.1 M  $\text{MgClO}_4$  (Aldrich) solution in acetonitrile (HPLC grade) as an electrolyte at room temperature under the protection of Nitrogen. The energy level relative to the vacuum level for the valence and conduction bands were determined through Eqs. (1) and (2).

$$E_{\text{VB}} = -e(E_{\text{Ox}} + 4.5) \quad (1)$$

$$E_{\text{CB}} = E_{\text{VB}} + E_{\text{BG}} \quad (2)$$

where  $E_{\text{VB}}$  is the valence band energy,  $E_{\text{CB}}$  is the conduction band energy,  $E_{\text{BG}}$  is the band-gap, and  $E_{\text{Ox}}$  the onset of oxidation potential.

### 2.4. Photocatalytic activity

The photocatalytic activity of the materials was evaluated by the degradation of Indigo Carmin dye, at a constant temperature of 320 K in a batch photo-reactor. Typically, 0.01 g of the materials was added in 30 ml of indigo carmine 25 mg L<sup>−1</sup> in the presence of 25  $\mu\text{L}$  of hydrogen peroxide 35% wt. The photodegradation was performed under a radiation  $\lambda > 400$  nm emitted from a mixed vapor lamp (160 W). The photocatalytic studies were also carried out in the absence of the materials prepared in order to evaluate the photocatalytic activity of the  $\text{H}_2\text{O}_2$  and carbon dots in the experimental conditions described. The UV-vis absorption measurements at  $\lambda = 610$  nm were used to monitor the indigo carmine dye photodegradation process. All measurements were performed using a UV-vis spectrometer Cary 50 (Varian). The degradation kinetics rate was determined with the Langmuir–Hinshelwood kinetic model [31]. This model has been extensively used for kinetics studies of photocatalytic degradation of organic compounds and dyes in heterogeneous photocatalysis [32].

## 3. Results and discussion

### 3.1. Characterizations of the carbon dots

The verification of emission of the HCD solution, when irradiated with UV light source, is the first evidence of HCD. The images of the solution under ambient and UV (365 nm) light are shown in Fig. 1. The solution under ambient light has a yellowish colour, whereas the solution irradiated com UV light presented an emission in the green region of the visible spectrum.

TEM and HRTEM images show the presence of agglomerates and isolated carbon nanostructures (Fig. 2a). A detailed analysis of these agglomerates clearly shows the presence of several nanoparticles with crystalline lattices characteristic of graphitic carbons (Fig. 2b).

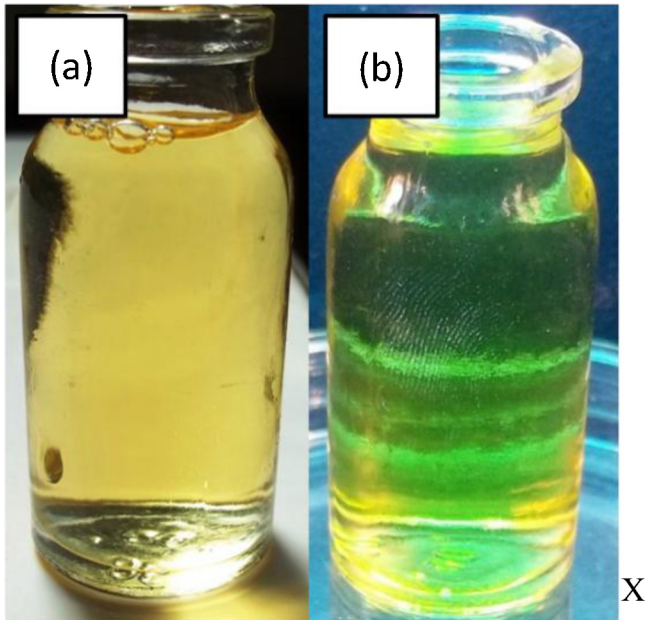


Fig. 1. Images of HCD solutions under ambient (a) and UV (b) light.

Fig. 3 shows the UV-vis spectrum obtained for the HCD solution. The HCD presented optical absorption in the UV region that extends to  $\sim 500$  nm. Based on the absorption spectrum, the photoluminescence spectra were obtained by excitation at wavelengths from 340 to 420 nm at 10 nm intervals. As shown in Fig. 3, the emissions are broad and excitation wavelength-dependent. The dependence of the fluorescence with the excitation wavelength can be result of different particle sizes or distributions of emission sites on the surface of the carbon dots [33].

The band structure of the carbon dots are highly dependent on surface groups as they can act as traps for electrons and holes [34]. Thus, it is necessary that the carbon dots have well-defined amounts of specific surface functional groups for coupling to occur between the band structures of the materials, in order to establish the heterojunction.

The characterization of the surface groups with FTIR, thermogravimetric analysis and potentiometric titration indicate the presence of large quantities of oxygenated functional groups introduced during the dehydration and oxidation reactions. The dehydration reaction with  $\text{H}_2\text{SO}_4$  proceeds until the aromatization/carbonization of the carbohydrate and  $\text{HNO}_3$  attacks the carbon surface eroding its structure and introducing oxygenated functional groups [35]. The FTIR spectrum shows the typical

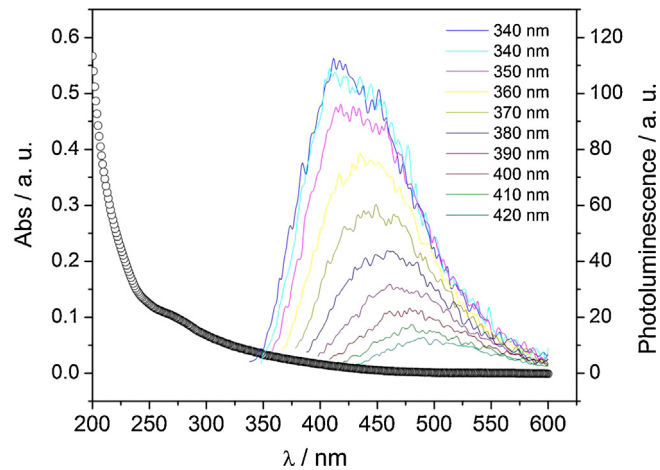


Fig. 3. UV-vis spectra (symbol) and photoluminescence spectra (solid line) with  $\lambda_{\text{ex}} = 340\text{--}420$  nm obtained for the HCD aqueous solution.

stretching of C—O ( $1100\text{ cm}^{-1}$ ), C=O ( $1600\text{ cm}^{-1}$  to  $1700\text{ cm}^{-1}$ ) and O—H at  $3350\text{ cm}^{-1}$  (Fig. 4). Asymmetric and symmetric stretching of  $\text{NO}_2$  occurs between  $1300$  and  $1550\text{ cm}^{-1}$ .

In addition, thermogravimetric and differential thermal analysis (Fig. S1) reinforce the interpretation of the FTIR spectrum with the identification of three well-defined exothermic events at  $380$ ,  $600$ , and  $850\text{ }^\circ\text{C}$  corresponding to the decomposition of oxygenated functional groups, nitro, carboxylic, lactones and quinones/phenols [29]. Table 1 shows the amount of such groups, determined by

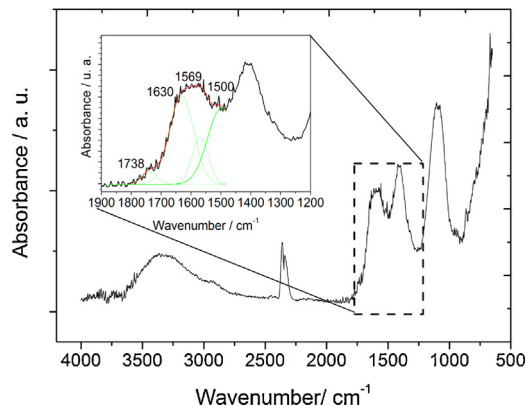


Fig. 4. HCD FTIR spectrum. Inset: deconvolution of the region located between  $1750$  and  $1250\text{ cm}^{-1}$ .

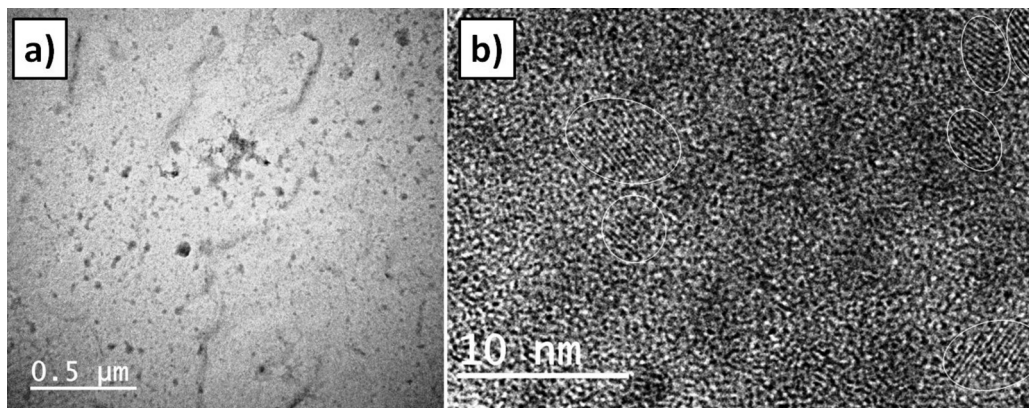
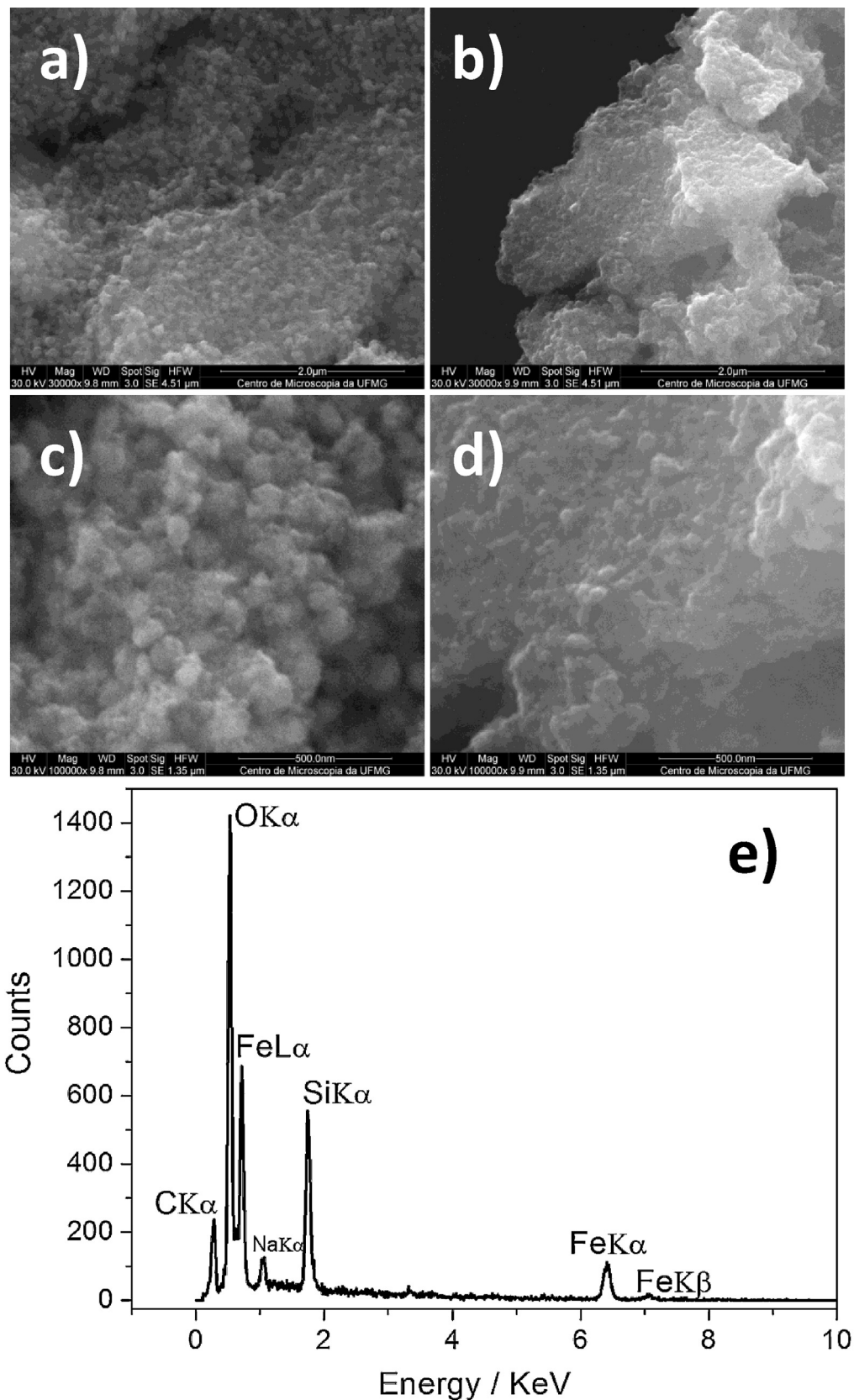


Fig. 2. TEM and HRTEM images of HCD prepared from acid dehydratation/oxidation.

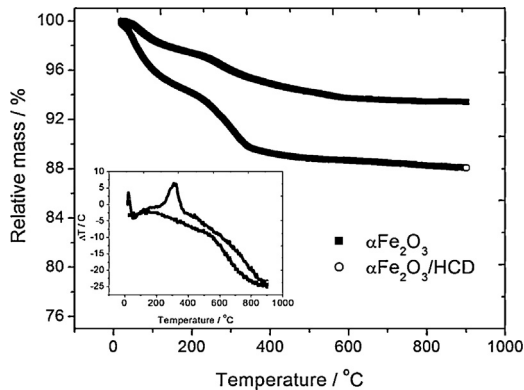


**Fig. 5.** SEM images of  $\alpha\text{Fe}_2\text{O}_3$  (a,c) and  $\alpha\text{Fe}_2\text{O}_3/\text{HCD}$  (b,d). EDS element data  $\alpha\text{Fe}_2\text{O}_3/\text{HCD}$  heterostructures (e).

**Table 1**

Surface property of the HCD prepared by dehydration/oxidation of cotton cellulose.

Oxygen surface groups/mmol g <sup>-1</sup>	Potential zeta/mV		
pK <sub>a</sub> < 5 3.2	5 < pK <sub>a</sub> < 8 0.54	pK <sub>a</sub> > 9 0.17	-19.2

**Fig. 6.** TG curves of  $\alpha\text{Fe}_2\text{O}_3$  and  $\alpha\text{Fe}_2\text{O}_3/\text{HCD}$  in  $\text{N}_2$  atmosphere. The inset shows the DTA results.

potentiometric titration curve adjustment (Fig. S2). The presence of this large amount of oxygenated acid groups is sufficient to generate a zeta potential of  $-19.2\text{ mV}$ . Using diffuse reflectance measurements and data manipulating with the Kubelka–Munk equation and the Tauc plot (Fig. S3), a direct transition band gap of  $2.7\text{ eV}$  was estimated for the prepared nanomaterials.

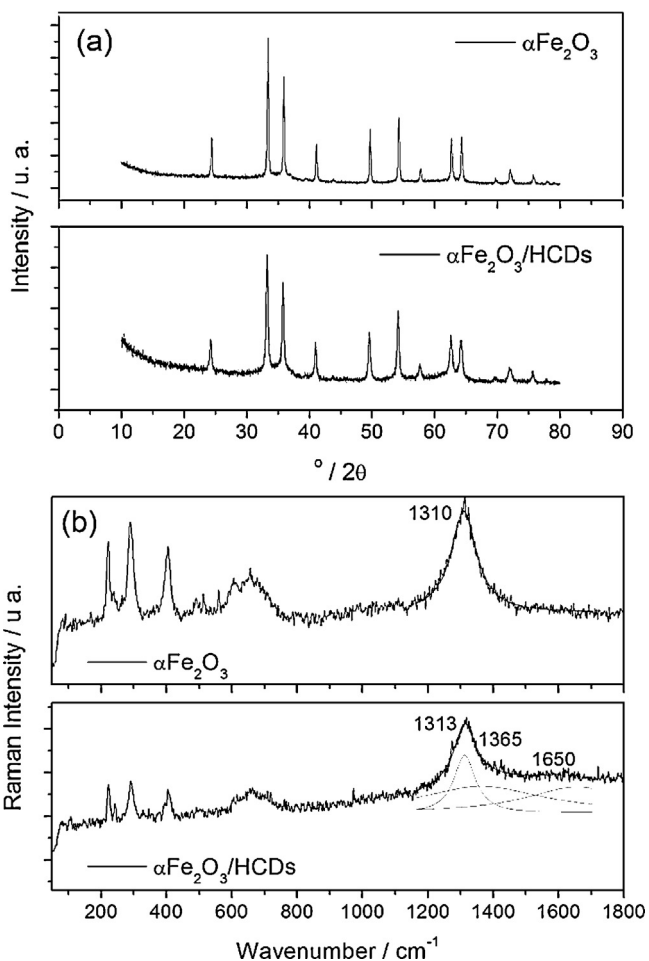
### 3.2. Characterization of $\alpha\text{Fe}_2\text{O}_3$ and hybrid $\alpha\text{Fe}_2\text{O}_3/\text{HCD}$

SEM images of the iron (III) oxide prepared are shown in Fig. 5a and c. The images reveal a spherical morphology with an average size of  $\sim 80\text{ nm}$ . Moreover, the smaller size of the iron (III) oxide particles prepared with the presence of the HCD can be noted (Fig. 5b and d). Energy Dispersive X-ray Spectroscopy (EDS) clearly shows the presence of carbon (Fig. 5e) in this sample.

Fig. 6 shows the TG curves for oxides prepared. Besides the weight loss characteristic of dehydration around  $100\text{ °C}$ , an accentuated weight loss around  $300\text{ °C}$  can be identified in the TG curve of the oxide prepared with HCD. At this temperature, the differential thermal analysis shows a positive temperature variation, characteristic of an exothermic event (Fig. 6). This mass loss may be interpreted as being due to the decomposition of carbon nanostructures of the material. Considering the differences in mass loss due to dehydration, the amount of HCDs anchored on oxide surface was estimated as being  $\sim 3.2\text{ wt\%}$ .

The crystal structure of the materials was investigated with XRD and Raman spectroscopy. Fig. 7 shows the diffraction pattern obtained for the iron (III) oxides prepared in aqueous medium. Both samples exhibit the typical diffraction peaks of  $\alpha\text{Fe}_2\text{O}_3$  (JCPDS CARD 33-664). The diffraction patterns are very similar, indicating that the synthesis of  $\alpha\text{Fe}_2\text{O}_3$  in the presence of HCD does not result in significant changes in its crystal structure.

The crystallite size was determined with the Scherrer equation using the peak centred at  $\sim 33.3\text{ }^{\circ}\text{2}\theta$ , corresponding to the plane 104. The values obtained were  $70$  and  $49\text{ nm}$  for  $\alpha\text{Fe}_2\text{O}_3$  and  $\alpha\text{Fe}_2\text{O}_3/\text{HCD}$ , respectively. We speculate that during the co-precipitation, HCD act as stabilizers of the newly formed  $\alpha\text{Fe}_2\text{O}_3$  nanoparticles, inhibiting their aggregation. As a result, the  $\alpha\text{Fe}_2\text{O}_3/\text{HCD}$  present smaller crystallites. Raman scattering spectrum (Fig. 7b) shows the typical vibrations of the alpha phase of iron (III) oxide at  $227, 292, 411, 497, 612, 659$ , and  $1310\text{ cm}^{-1}$  [36–38].

**Fig. 7.** X-ray diffraction patterns (a) and Raman spectrum (b) obtained for the prepared materials.

In the spectrum of the  $\alpha\text{Fe}_2\text{O}_3/\text{HCD}$  sample there is an asymmetric in the band scattering located at  $1310\text{ cm}^{-1}$ . This asymmetry is attributed to scattering of graphitic structures, specifically the bands G ( $\sim 1600\text{ cm}^{-1}$ ) and D ( $\sim 1350\text{ cm}^{-1}$ ). The FTIR spectrum (Fig. S4) of the composite shows stretching vibrations of C=O and C=C between  $1750$  and  $1500\text{ cm}^{-1}$  originating from different functional groups found in the HCD, in addition to the typical vibration of the  $\alpha\text{Fe}_2\text{O}_3$  prepared in aqueous medium [28].

Fitting the room temperature ( $\sim 298\text{ K}$ )  $^{57}\text{Fe}$ -Mössbauer spectrum (Fig. 8a) for this synthetic hematite ( $\alpha\text{Fe}_2\text{O}_3$ ) sample with a hyperfine field distribution leads to a probability profile (61.1% of the relative spectral area, RA) with three main maxima Fig. S5a, with an averaged quadrupole shift,  $2\epsilon = 0.215\text{ mm s}^{-1}$ . One of them is centered at the characteristic hyperfine field value (51.9 tesla) for a bulk pure  $\alpha\text{Fe}_2\text{O}_3$ . Two other maxima are centered at 51.0 tesla and 49.4 tesla, which may be interpreted as being due to collective magnetic relaxation, implying a linear temperature dependence of the magnetic hyperfine field [39], according to the different pure  $\alpha\text{Fe}_2\text{O}_3$  particle sizes. A fraction of still finer particles, certainly with diameters not higher than  $15\text{ nm}$  as it can be directly deduced from data by Bødker and Mørup [40], which undergo superparamagnetic relaxation [41], accounts for the broad central and asymmetric central doublet in the spectrum. Fitting it with a numerical model of quadrupole splitting distribution (RA = 38.9%) leads to the probability profile of Figure S5b. A similar analysis of the spectrum (Fig. 8b) for the sample of hematite with carbon dots gives the probability profile of Fig. S6a (RA = 53.5%), that also shows three main maxima. The maximum centered at the hyperfine field value

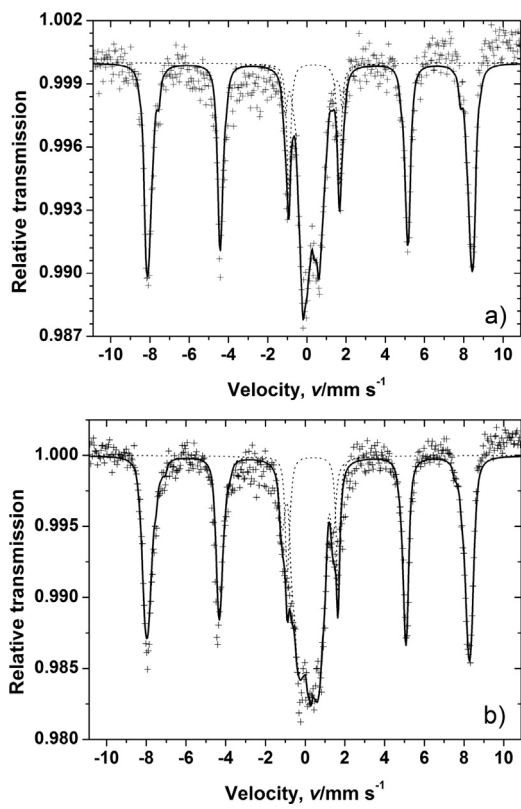


Fig. 8.  $^{57}\text{Fe}$ -Mossbauer patterns at 298 K. (a)  $\alpha\text{Fe}_2\text{O}_3$  and (b)  $\alpha\text{Fe}_2\text{O}_3/\text{HCD}$ .

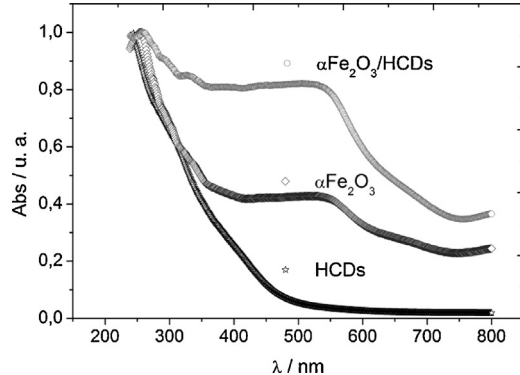


Fig. 9. UV-vis spectra obtained for HCD,  $\alpha\text{Fe}_2\text{O}_3$  and  $\alpha\text{Fe}_2\text{O}_3/\text{HCD}$ . The absorbance values were obtained with the Kubelka–Munk function and normalized to the maximum absorption.

of 51.1 tesla may still be assigned to a bulk pure  $\alpha\text{Fe}_2\text{O}_3$ . Two other are centered at 50.0 tesla and 48.9 tesla due to collective magnetic relaxation. Moreover, the effect of collective magnetic relaxation particles in this sample would be slightly smaller than the corresponding fractions of the sample of this pure  $\alpha\text{Fe}_2\text{O}_3$ . The quadrupole splitting distribution profile (Fig. S6b); RA = 46.6%) is somewhat distinguishable from the corresponding pattern for the pure  $\alpha\text{Fe}_2\text{O}_3$ , but would still account for the fraction of very small particle sizes undergoing superparamagnetic relaxation.

The electronic band structure and optical properties of materials were investigated using cyclic voltammetry and UV-vis spectroscopy. Fig. 9 shows the electronic spectra obtained for these materials.

Moreover, the absorption capacity increases significantly at  $\lambda > 350$  nm. From the Tauc plot analysis (Fig. S7), the direct transition band gaps were estimated to be 2.0 and 1.7 eV for  $\alpha\text{Fe}_2\text{O}_3$  and

Table 2

Optical band gap as obtained by UV-vis spectroscopy. Top of the valence band and bottom of the conduction band energy obtained from cyclic voltammetry data.

	Band gap (optical)/eV	Valence band/eV	Conduction band/eV
HCD	2.7	-6.3	-3.6
$\alpha\text{Fe}_2\text{O}_3$	2.0	-6.9	-4.9
$\alpha\text{Fe}_2\text{O}_3/\text{HCD}$	1.7	-6.5	-4.8

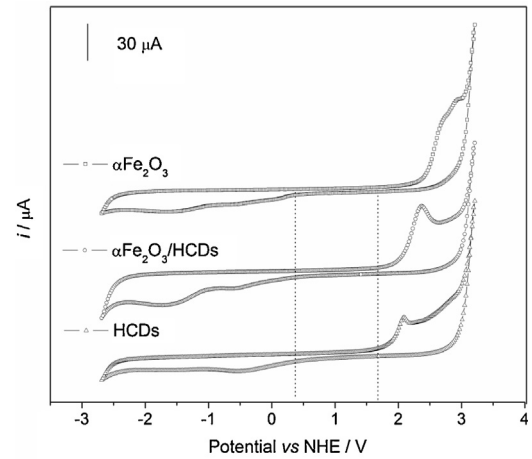
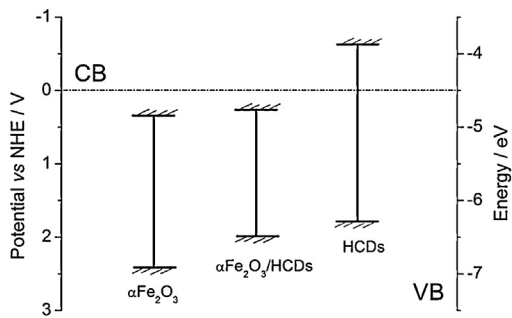


Fig. 10. Typical cyclic voltammograms obtained for materials deposited on GC work electrode using 0.1 M  $\text{MgClO}_4$ /acetonitrile as electrolyte support.

$\alpha\text{Fe}_2\text{O}_3/\text{HCD}$ , respectively (Table 2). The presence of HCD causes a decrease in the band gap of hematite. To better understand these results, the energy level relatively to the vacuum level of the top of the valence band and of the bottom of the conduction band was investigated with cyclic voltammetry. Fig. 10 shows typical cyclic voltammograms obtained for the HCD,  $\alpha\text{Fe}_2\text{O}_3$  and  $\alpha\text{Fe}_2\text{O}_3/\text{HCD}$ . The  $\alpha\text{Fe}_2\text{O}_3$  shows typical onset of oxidation potential at 2.43 V [42]. The HCD present an onset of oxidation potential ( $E_{\text{OX}}$ ) at  $\sim 1.8$  V (Table 2). Wang et al. observed an  $E_{\text{OX}}$  of 0.80 V with carbon dots synthesized in non-coordinating solvent [43]. Pan et al. found an  $E_{\text{OX}}$  close to 1.2 V for graphene-quantum-dots [44]. The HCD prepared here are highly oxidized so there is a greater difficulty in promoting their oxidation. The presence of oxygen functional groups significantly interferes in the band structure changing the energy of the valence and conduction band, and of the work function [45]. The hybrid nanocomposite presents an intermediate  $E_{\text{OX}}$  (Table 2). These results, added to those obtained with UV-vis spectroscopy, that is, reduced band gap and increased radiation absorption, suggest that in the hybrid material, the electrons are ejected from both hematite and HCD valence band. The increased radiation absorption capacity can also be related to the increased surface area of the  $\alpha\text{Fe}_2\text{O}_3/\text{HCD}$  sample, as a result of the smaller particle size of the oxide in association with the anchoring of carbon nanoparticles [14,19,23].

Fig. 11 shows the energy level relatively to the vacuum level for their respective redox potential. It can be seen that the bands of the materials exhibit Type II band offsets. The heterostructures comprised of photoactive materials exhibiting Type II band offsets are able to promote the efficient separation of photogenerated charges under irradiation [46]. On coupling, the electrons are excited from the valence band of the HCD to the conduction band of the hematite and vice versa. On the other hand, the excited electrons present in the hematite conduction band can decay to the energy levels of the HCD valence band. Similarly, the excited electrons present in the HCD conduction band, may be carried forward by the hematite band structure. In both cases there are distinct mechanisms to explain the low recombination low.



**Fig. 11.** Relationship between the energy of the band structure and redox potentials of HCD,  $\alpha\text{Fe}_2\text{O}_3$  and  $\alpha\text{Fe}_2\text{O}_3/\text{HCDs}$ .

### 3.3. Photocatalytic activity

To evaluate the photocatalytic activity of these materials the photodegradation of indigo carmine dye was used as a molecule model. **Fig. 12** shows all the spectra resulting from the photocatalysis of this dye.

**Fig. 13** shows the relative concentrations of the dye as a function of photocatalysis time. The photocatalytic differences are evident. The hydrogen peroxide irradiated with visible light does not cause major changes, since hydroxyl radicals are not formed. Similar results were obtained with HCD and  $\alpha\text{Fe}_2\text{O}_3$ . Several studies show that hematite, despite of absorbing more solar spectrum radiation, has a fast electron-hole recombination which significantly reduces its photocatalytic activity [7].

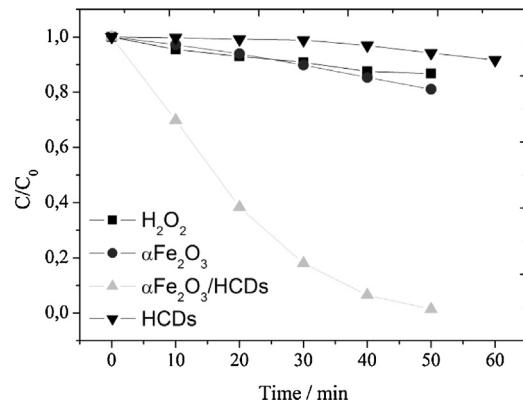


**Fig. 13.** Photocatalytic activity of the materials prepared in the degradation of indigo carmine.

Zhou et al. [47] showed that the photocatalytic efficiency can be modified with different  $\alpha\text{Fe}_2\text{O}_3$  morphologies (nanoplates, nanocubes and nanorods). In that work the authors have shown that the nanorod shapes have strong activity on degrading RhB dye due to exposure of the crystal facets with high  $\text{Fe}^{3+}$  density. As a result, there is a significant increase in the formation of hydroxyl radicals via the redox cycle between  $\text{Fe}^{3+}$  and  $\text{Fe}^{2+}$  [47]. On the other hand, hybrid nanocomposites showed high photocatalytic activity in the degradation of indigo carmine dye. The preparation of hybrid  $\alpha\text{Fe}_2\text{O}_3$  nanocomposites and carbon dots for photocatalysis was recently reported without a clear explanation of the reaction mech-

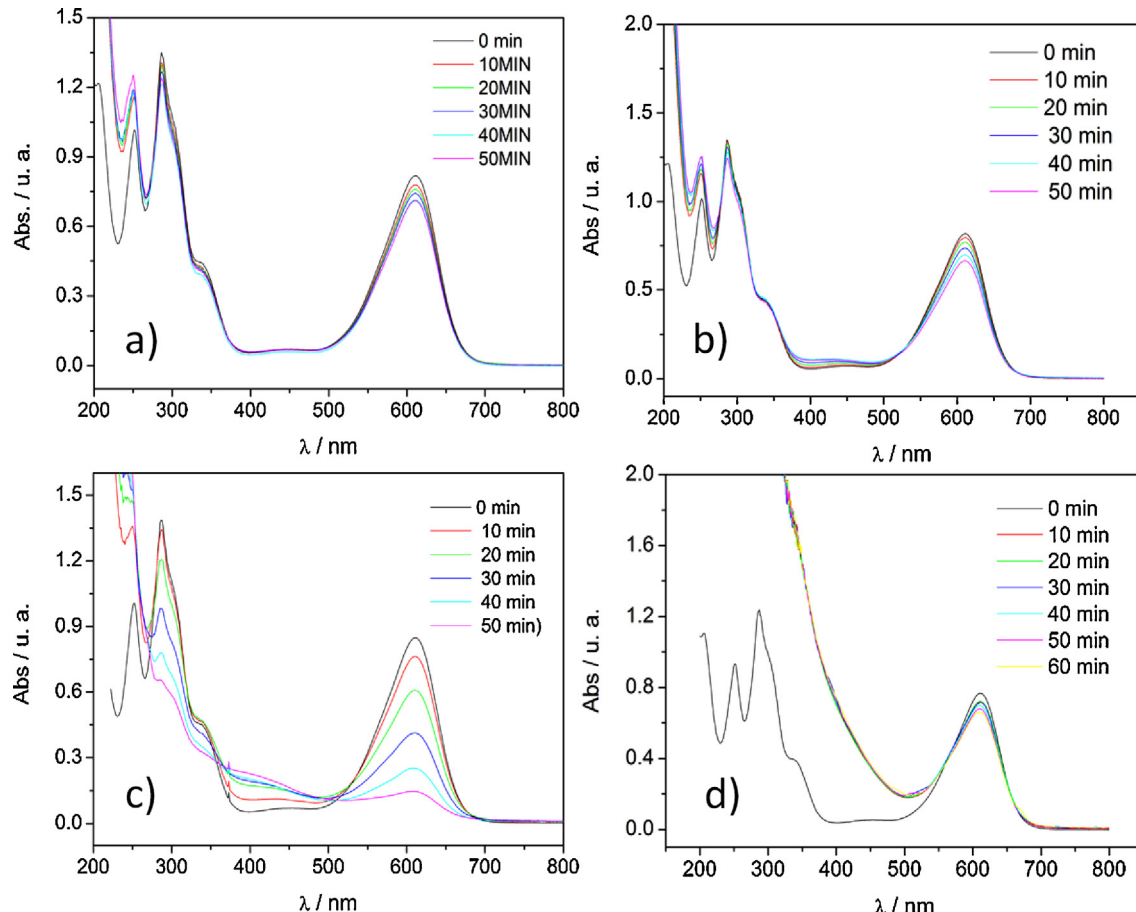


**Fig. 12.** UV-vis spectra of indigo carmine dye during photocatalysis. (a)  $\text{H}_2\text{O}_2$  (25  $\mu\text{L}$ ), (b)  $\alpha\text{Fe}_2\text{O}_3$  with  $\text{H}_2\text{O}_2$  (25  $\mu\text{L}$ ), (c)  $\alpha\text{Fe}_2\text{O}_3/\text{HCD}$  with  $\text{H}_2\text{O}_2$  (25  $\mu\text{L}$ ), (d) HCD with  $\text{H}_2\text{O}_2$  (25  $\mu\text{L}$ ).

**Table 3**

Pseudo first order rate constants ( $K_{app}$ ) and their respective correlation coefficients ( $R^2$ ) obtained for the photodegradation with  $\alpha\text{Fe}_2\text{O}_3$ ,  $\text{H}_2\text{O}_2$ , HCD and  $\alpha\text{Fe}_2\text{O}_3/\text{HCD}$ .

	$K_{app}/\text{min}^{-1}$	$R^2$
$\alpha\text{Fe}_2\text{O}_3/\text{HCD}$	$6.8 \times 10^{-2}$	0.98
$\text{H}_2\text{O}_2$	$3.1 \times 10^{-3}$	0.94
$\alpha\text{Fe}_2\text{O}_3$	$4.5 \times 10^{-3}$	0.99
HCD	$1.4 \times 10^{-3}$	0.93

anism provided by the photocatalyst [19,23]. Zhang et al. reported the easy one-step preparation of hematite with carbon quantum dots ( $\alpha\text{Fe}_2\text{O}_3/\text{CQD}$ ) nanocomposites and evaluated their photocatalytic performance on the degradation of benzene and methanol in gas-phase under visible light. The authors speculated that the CQD increase the concentration of toxic molecules on the surface of the photocatalyst, decrease the electron-hole recombination rate and increase the amount of excited electrons in  $\alpha\text{Fe}_2\text{O}_3$  as a result of their upconversion photoluminescence property [19]. Similar discussion was presented by You and Young Kwak on the photodegradation of MB aqueous solutions with carbon quantum dots embedded with mesoporous hematite nanospheres [22]. From the present results, it is believed that the high photocatalytic activity observed for  $\alpha\text{Fe}_2\text{O}_3/\text{HCD}$  is directly related to the formation of heterostructures. On forming the heterojunction, the electrons are excited from both the valence band of  $\alpha\text{Fe}_2\text{O}_3$  and the HCD. In addition, the recombination rate is reduced, as the excited electrons can transit through the band structure of both materials. Thus, there is a significant increase of the generated oxidative radicals which results in rapid degradation/mineralization of the dye [48]. On absorbing the visible light ( $\lambda > 400 \text{ nm}$ ), the electrons are excited from the top of the valence band of the iron oxide and HCD to the bottom of the conduction band of the  $\alpha\text{Fe}_2\text{O}_3$ . The generated electrons on the structure surface interact with  $\text{H}_2\text{O}_2$  and with the  $\text{O}_2$  adsorbed on the surface to generate hydroxyl radicals and oxygen radicals ( $\cdot\text{O}_2^-$ ), respectively. Interactions between  $\text{OH}^-$  and the holes also lead to the formation of radicals that attack the dye bonds leading to degradation/mineralization. The degradation kinetics rate was determined through the Langmuir–Hinshelwood kinetic model (Eq. (3)) [31].

$$\ln \left( \frac{C_0}{C_t} \right) = kK_{\text{cor}}t = K_{\text{ap}}t \quad (3)$$

The obtained results from the linear regression (Fig. S8) are summarized in Table 3. The photodegradation rate of the hybrid nanocomposite is one order of magnitude higher than the  $\alpha\text{Fe}_2\text{O}_3$ , HCD and  $\text{H}_2\text{O}_2$ , which individually presents very low activity under visible light.

#### 4. Conclusions

$\alpha\text{Fe}_2\text{O}_3/\text{HCD}$  heterostructures were prepared by co-precipitation of iron oxide in HCD aqueous solution. The surface properties of the HCD prepared were essential for the coupling of the materials bands structures. Additionally, the hydrophilic functional group on the surface of the HCD interacts with  $\alpha\text{Fe}_2\text{O}_3$  nanoparticles during co-precipitation inhibiting the aggregation, resulting in smaller lower nanostructures with larger surface area. The increased surface area combined with the synergism in light absorption and decreased recombination rate occasioned by the establishment of a hybrid heterojunction, have generated an exceptional improvement in the indigo carmine dye photodegradation under visible light. The analysis of the band structure provided clear evidence of the coupling bands of the material justifying the greater ability to absorb light and decrease the band gap energy of the hybrid material favoring the charge separation and the charge recombination suppression. Thus, these results can

impact on the design of new photocatalytic heterojunctions based on carbon dots and/or iron oxides. For example, the properties related to the HCD (surface functionalization, particle size) can be optimized so that better results can be achieved. Finally, we believe that the results obtained are the starting point for obtaining a hybrid based on iron oxides and HCD activated by visible light, which are inexpensive and have a high capacity for photo-mineralizing of recalcitrant substances and water splitting to produce hydrogen and oxygen. In future work, our goals will be the coupling optimization of the band structure of the materials for water splitting.

#### Acknowledgements

The authors wish to thanks CAPES, FAPEMIG (Process APQ-00614-13), RQ-MG and CNPq (grants # 478228/2013-9 and 305755/2013-7) for the financial support. JDF thanks CAPES for granting his visiting professorship at the Federal University of the Jequitinhonha and Mucury Valleys, in Diamantina, Minas Gerais, Brazil.

#### Appendix A. Supplementary data

Supplementary data associated with this article can be found, in the online version, at <http://dx.doi.org/10.1016/j.apcatb.2015.09.036>.

#### References

- [1] J.S. Jang, H.G. Kim, J.S. Lee, Heterojunction semiconductors: a strategy to develop efficient photocatalytic materials for visible light water splitting, *Catal. Today* 185 (2012) 270–277.
- [2] C.X. Kronawitter, L. Vayssières, S. Shen, L. Guo, D.A. Wheeler, J.Z. Zhang, B.R. Antoun, S.S. Mao, A perspective on solar-driven water splitting with all-oxide hetero-nanostructures, *Energy Environ. Sci.* 4 (2011) 3889–3899.
- [3] H.D.S. Oliveira, A.C. Silva, J.P. de Mesquita, F.V. Pereira, D.Q. Lima, J.D. Fabris, F.C.C. Moura, L.C.A. Oliveira, A novel floating photocatalyst device based on cloth canvas impregnated with iron oxide, *New J. Chem.* 37 (2013) 2486–2491.
- [4] I.S.X. Pinto, P.H.V.V. Pacheco, J.V. Coelho, E. Lorençon, J.D. Ardisson, J.D. Fabris, P.P. de Souza, K.W.H. Krambrock, L.C.A. Oliveira, M.C. Pereira, Nanostructured  $\delta\text{-FeOOH}$ : an efficient Fenton-like catalyst for the oxidation of organics in water, *Appl. Catal. B: Environ.* 119–120 (2012) 175–182.
- [5] X.-L. Fang, C. Chen, M.-S. Jin, Q. Kuang, Z.-X. Xie, S.-Y. Xie, R.-B. Huang, L.-S. Zheng, Single-crystal-like hematite colloidal nanocrystal clusters: synthesis and applications in gas sensors, photocatalysis and water treatment, *J. Mater. Chem.* 19 (2009) 6154–6160.
- [6] L. Li, N. Koshizaki, Vertically aligned and ordered hematite hierarchical columnar arrays for applications in field-emission, superhydrophilicity, and photocatalysis, *J. Mater. Chem.* 20 (2010) 2972–2978.
- [7] K. Sivula, F. Le Formal, M. Grätzel, Solar water splitting: progress using hematite ( $\alpha\text{-Fe}_2\text{O}_3$ ) photoelectrodes, *ChemSusChem* 4 (2011) 432–449.
- [8] K. Sivula, R. Zboril, F. Le Formal, R. Robert, A. Weidenkaff, J. Tucek, J. Frydrych, M. Grätzel, Photoelectrochemical water splitting with mesoporous hematite prepared by a solution-based colloidal approach, *J. Am. Chem. Soc.* 132 (2010) 7436–7444.
- [9] J.H. Kennedy, K.W. Frese, Photooxidation of water at  $\alpha\text{-Fe}_2\text{O}_3$  electrodes, *J. Electrochem. Soc.* 125 (1978) 709–714.
- [10] K. Sivula, F.L. Formal, M. Grätzel,  $\text{WO}_3\text{-Fe}_2\text{O}_3$  photoanodes for water splitting: a host Scaffold, guest absorber approach, *Chem. Mater.* 21 (2009) 2862–2867.
- [11] Y. Wang, T. Yu, X. Chen, H. Zhang, S. Ouyang, Z. Li, J. Ye, Z. Zou, Enhancement of photoelectric conversion properties of  $\text{SrTiO}_3/\alpha\text{-Fe}_2\text{O}_3$  heterojunction photoanode, *J. Phys. D: Appl. Phys.* 40 (2007) 3925.
- [12] W. Luo, T. Yu, Y. Wang, Z. Li, J. Ye, Z. Zou, Enhanced photocurrent–oltage characteristics of  $\text{WO}_3/\text{Fe}_2\text{O}_3$  nano-electrodes, *J. Phys. D: Appl. Phys.* 40 (2007) 1091.
- [13] J.J.M. Vequizo, M. Ichimura, Fabrication of  $\text{Cu}_2\text{O}/\delta\text{-FeOOH}$  heterojunction solar cells using electrodeposition, *Appl. Phys. Express* 7 (2014) 045501.
- [14] F. Meng, J. Li, S.K. Cushing, J. Bright, M. Zhi, J.D. Rowley, Z. Hong, A. Manivannan, A.D. Bristow, N. Wu, Photocatalytic water oxidation by hematite/reduced graphene oxide composites, *ACS Catal.* 3 (2013) 746–751.
- [15] X. Xu, R. Ray, Y. Gu, H.J. Ploehn, L. Gearheart, K. Raker, W.A. Scrivens, Electrophoretic analysis and purification of fluorescent single-walled carbon nanotube fragments, *J. Am. Chem. Soc.* 126 (2004) 12736–12737.
- [16] J.C.G. Esteves da Silva, H.M.R. Gonçalves, Analytical and bioanalytical applications of carbon dots, *Trac-Trends Anal. Chem.* 30 (2011) 1327–1336.

[17] H. Li, X. He, Z. Kang, H. Huang, Y. Liu, J. Liu, S. Lian, C.H.A. Tsang, X. Yang, S.-T. Lee, Water-soluble fluorescent carbon quantum dots and photocatalyst design, *Angew. Chem. Int. Ed.* 49 (2010) 4430–4434.

[18] S.N. Baker, G.A. Baker, Luminous carbon nanodots: emergent nanolights, *Angew. Chem. Int. Ed.* 49 (2010) 6726–6744.

[19] H. Zhang, H. Ming, S. Lian, H. Huang, H. Li, L. Zhang, Y. Liu, Z. Kang, S.-T. Lee,  $\text{Fe}_2\text{O}_3$ /carbon quantum dots complex photocatalysts and their enhanced photocatalytic activity under visible light, *Dalton Trans.* 40 (2011) 10822–10825.

[20] H. Ming, Z. Ma, Y. Liu, K. Pan, H. Yu, F. Wang, Z. Kang, Large scale electrochemical synthesis of high quality carbon nanodots and their photocatalytic property, *Dalton Trans.* 41 (2012) 9526–9531.

[21] H. Yu, H. Zhang, H. Huang, Y. Liu, H. Li, H. Ming, Z. Kang,  $\text{ZnO}$ /carbon quantum dots nanocomposites: one-step fabrication and superior photocatalytic ability for toxic gas degradation under visible light at room temperature, *New J. Chem.* 36 (2012) 1031–1035.

[22] A. Safavi, F. Sedaghati, H. Shahbaazi, E. Farjam, Facile approach to the synthesis of carbon nanodots and their peroxidase mimetic function in azo dyes degradation, *RSC Adv.* 2 (2012) 7367–7370.

[23] B.Y. Yu, S.-Y. Kwak, Carbon quantum dots embedded with mesoporous hematite nanospheres as efficient visible light-active photocatalysts, *J. Mater. Chem.* 22 (2012) 8345–8353.

[24] J. Wang, S. Sahu, S.K. Sonkar, K.N. Tackett II, K.W. Sun, Y. Liu, H. Maimaiti, P. Anilkumar, Y.-P. Sun, Versatility with carbon dots—from overcooked BBQ to brightly fluorescent agents and photocatalysts, *RSC Adv.* 3 (2013) 15604–15607.

[25] S.-T. Yang, L. Cao, P.G. Luo, F. Lu, X. Wang, H. Wang, M.J. Meziani, Y. Liu, G. Qi, Y.-P. Sun, Carbon dots for optical imaging in vivo, *J. Am. Chem. Soc.* 131 (2009) 11308–11309.

[26] S.-T. Yang, X. Wang, H. Wang, F. Lu, P.G. Luo, L. Cao, M.J. Meziani, J.-H. Liu, Y. Liu, M. Chen, Y. Huang, Y.-P. Sun, Carbon dots as nontoxic and high-performance fluorescence imaging agents, *J. Phys. Chem. C* 113 (2009) 18110–18114.

[27] H. Peng, J. Trivas-Sejdic, Simple aqueous solution route to luminescent carbogenic dots from carbohydrates, *Chem. Mater.* 21 (2009) 5563–5565.

[28] R.M. Cornell, U. Schwertmann, *The Iron Oxides: Structure, Properties, Reactions, Occurrences and Uses*, Wiley, 2003, 2015.

[29] H.F. Gorgulho, J.P. Mesquita, F. Gonçalves, M.F.R. Pereira, J.L. Figueiredo, Characterization of the surface chemistry of carbon materials by potentiometric titrations and temperature-programmed desorption, *Carbon* 46 (2008) 1544–1555.

[30] J.P. de Mesquita, P.B. Martelli, H.D.F. Gorgulho, Characterization of copper adsorption on oxidized activated carbon, *J. Braz. Chem. Soc.* 17 (2006) 1133–1143.

[31] H. Al-Ekabi, N. Serpone, Kinetics studies in heterogeneous photocatalysis. I. Photocatalytic degradation of chlorinated phenols in aerated aqueous solutions over titania supported on a glass matrix, *J. Phys. Chem.* 92 (1988) 5726–5731.

[32] H.R. Rajabi, O. Khani, M. Shamsipur, V. Vatanpour, High-performance pure and  $\text{Fe}^{3+}$ -ion doped  $\text{ZnS}$  quantum dots as green nanophotocatalysts for the removal of malachite green under UV-light irradiation, *J. Hazard. Mater.* 250–251 (2013) 370–378.

[33] S.Y. Lim, W. Shen, Z. Gao, Carbon quantum dots and their applications, *Chem. Soc. Rev.* 44 (2015) 362–381.

[34] Y. Wang, A. Hu, Carbon quantum dots: synthesis, properties and applications, *J. Mater. Chem. C* 2 (2014) 6921–6939.

[35] I. Gerber, M. Oubenali, R. Bacsa, J. Durand, A. Gonçalves, M.F.R. Pereira, F. Jolibois, L. Perrin, R. Poteau, P. Serp, Theoretical and experimental studies on the carbon-nanotube surface oxidation by nitric acid: interplay between functionalization and vacancy enlargement, *Chem.: Eur. J.* 17 (2011) 11467–11477.

[36] D.L.A. de Faria, S. Venâncio Silva, M.T. de Oliveira, Raman microspectroscopy of some iron oxides and oxyhydroxides, *J. Raman Spectrosc.* 28 (1997) 873–878.

[37] D.L.A. de Faria, F.N. Lopes, Heated goethite and natural hematite: can Raman spectroscopy be used to differentiate them? *Vibrational Spectrosc.* 45 (2007) 117–121.

[38] Y.-S. Li, J.S. Church, A.L. Woodhead, Infrared and Raman spectroscopic studies on iron oxide magnetic nano-particles and their surface modifications, *J. Magn. Magn. Mater.* 324 (2012) 1543–1550.

[39] S. Mørup, M.F. Hansen, C. Frandsen, Magnetic interactions between nanoparticles, *Beilstein J. Nanotechnol.* 1 (2010) 182–190.

[40] F. Bodker, S. Mørup, Size dependence of the properties of hematite nanoparticles, *EPL (Europhys. Lett.)* 52 (2000) 217.

[41] S. Mørup, H. Topsøe, Mössbauer studies of thermal excitations in magnetically ordered microcrystals, *Appl. Phys.* 11 (1976) 63–66.

[42] M. Gratzel, Photoelectrochemical cells, *Nature* 414 (2001) 338–344.

[43] F. Wang, Y.-H. Chen, C.-Y. Liu, D.-G. Ma, White light-emitting devices based on carbon dots' electroluminescence, *Chem. Commun.* 47 (2011) 3502–3504.

[44] D. Pan, C. Xi, Z. Li, L. Wang, Z. Chen, B. Lu, M. Wu, Electrophoretic fabrication of highly robust, efficient, and benign heterojunction photoelectrocatalysts based on graphene-quantum-dot sensitized  $\text{TiO}_2$  nanotube arrays, *J. Mater. Chem. A* 1 (2013) 3551–3555.

[45] H. Ago, T. Kugler, F. Cacialli, W.R. Salaneck, M.S.P. Shaffer, A.H. Windle, R.H. Friend, Work functions and surface functional groups of multiwall carbon nanotubes, *J. Phys. Chem. B* 103 (1999) 8116–8121.

[46] H. Zhong, Y. Zhou, Y. Yang, C. Yang, Y. Li, Synthesis of type II  $\text{CdTe}$ – $\text{CdSe}$  nanocrystal heterostructured multiple-branched rods and their photovoltaic applications, *J. Phys. Chem. C* 111 (2007) 6538–6543.

[47] X. Zhou, J. Lan, G. Liu, K. Deng, Y. Yang, G. Nie, J. Yu, L. Zhi, Facet-mediated photodegradation of organic dye over hematite architectures by visible light, *Angew. Chem. Int. Ed.* 51 (2012) 178–182.

[48] W.F. de Souza, I.R. Guimarães, M.C. Guerreiro, L.C.A. Oliveira, Catalytic oxidation of sulfur and nitrogen compounds from diesel fuel, *Appl. Catal. A: Gen.* 360 (2009) 205–209.